

# Phase-Separated Nanophotonic Structures by Inkjet Printing

Yidenekachew J. Donie,\* Stefan Schlisske, Radwanul H. Siddique, Adrian Mertens, Vinayak Narasimhan, Fabian Schackmar, Manuel Pietsch, Ihtez M. Hossain, Gerardo Hernandez-Sosa, Uli Lemmer,\* and Guillaume Gomard\*



Cite This: *ACS Nano* 2021, 15, 7305–7317



Read Online

ACCESS |



Metrics & More



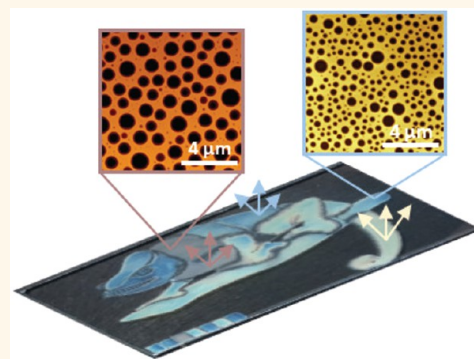
Article Recommendations



Supporting Information

**ABSTRACT:** The spontaneous phase separation of two or more polymers is a thermodynamic process that can take place in both biological and synthetic materials and which results in the structuring of the matter from the micro- to the nanoscale. For photonic applications, it allows forming quasi-periodic or disordered assemblies of light scatterers at high throughput and low cost. The wet process methods currently used to fabricate phase-separated nanostructures (PSNs) limit the design possibilities, which in turn hinders the deployment of PSNs in commercialized products. To tackle this shortcoming, we introduce a versatile and industrially scalable deposition method based on the inkjet printing of a polymer blend, leading to PSNs with a feature size that is tuned from a few micrometers down to sub-100 nm. Consequently, PSNs can be rapidly processed into the desired macroscopic design. We demonstrate that these printed PSNs can improve light management in manifold photonic applications, exemplified here by exploiting them as a light extraction layer and a metasurface for light-emitting devices and point-of-care biosensors, respectively.

**KEYWORDS:** phase-separated nanostructures, inkjet printing, light management, biosensing, printed electronics, printed biosensors



Phase separation is a process whereby a single-phase homogeneous solution demixes into two or more distinct phases.<sup>1,2</sup> Our everyday experience with water and oil droplets illustrates such a spontaneous liquid–liquid phase separation. In living cells, it can result in the formation of a variety of cytoplasmic structures like networks, sheets, cylinders, spheres, tubules, and filaments.<sup>3</sup> In some bird and arthropod species, structural colors are thus generated when light is scattered by phase-separated nanostructures (PSNs) in biological tissues.<sup>4,5</sup> At the same time, there have been worldwide collaborative efforts between the fundamental and applied science communities to exploit phase-separation processes in bioinspired synthetic materials, formed out of modified biomaterials,<sup>6</sup> biodegradable,<sup>7</sup> conductive,<sup>8</sup> and nonconductive polymers<sup>1,2</sup> as well as inorganic nanocomposites.<sup>9</sup> These synthetic PSNs find applications in many research fields including cell biology, tissue engineering, drug delivery and medicinal science, optics, and electronics. In particular, the attractiveness of phase-separation processes for optics and electronics (highlighted in Table 1) results from their capacity to generate fine patterns (e.g., with a feature size <100 nm) at high throughput and low cost.<sup>10,11</sup> The successful transfer of PSNs from lab-scale demonstrators into real-world products will depend on the possibility to easily form these micro-/

**Table 1. Examples of Phase-Separated Nanostructures Processed by Spin-Coating**

application/optical material	feature size (nm)
magnetic recording device <sup>14,15</sup>	<50
field effect transistor <sup>16,17</sup>	<30
phase change memory <sup>18</sup>	<20
nanocrystal memory device <sup>19</sup>	20
laser diodes <sup>20</sup>	20
MOS capacitor <sup>21</sup>	20
metasurfaces <sup>22,23</sup>	<200
antireflective coating <sup>24,25</sup>	<100
photonic band gap material <sup>26,27</sup>	50–500
optical filter <sup>28</sup>	<160
sensor (pressure, <sup>27,29</sup> protein, DNA, <sup>30</sup> RNA <sup>31</sup> )	200–800
solar cells <sup>32–34</sup>	40–600
OLEDs <sup>35</sup>	200–1000
photodiodes <sup>8</sup>	10000–15000

Received: January 20, 2021

Accepted: April 7, 2021

Published: April 12, 2021



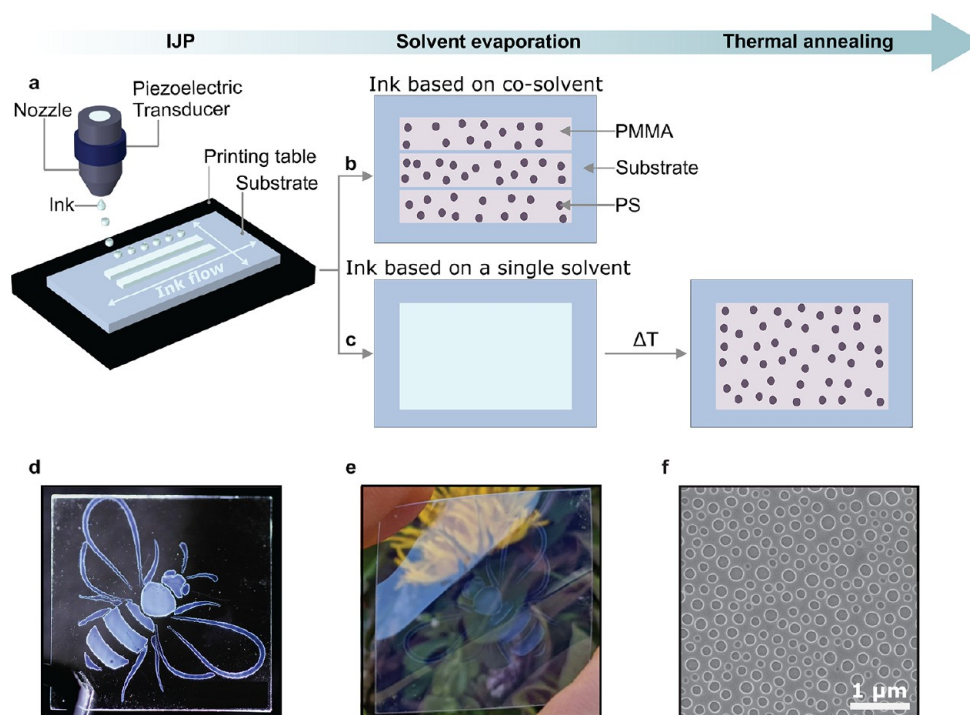


**Figure 1.** IJP enables the direct writing of PSNs in complex designs and over diverse substrates. Schematic illustration of the key steps involved in IJP of the PS/PMMA = 30:70 ink: (a) inkjet printing of an ink based on (b) cyclohexanone and Tetralin, (c) only cyclohexanone. (b) and (c) schematics depict the resulting films after the solvent evaporation at room temperature. The PSNs are formed during solvent evaporation for (b), and for (c) only after thermal annealing as depicted in the schematics. (d) Photograph of an IJP 25 mm  $\times$  25 mm glass substrate illuminated by a white LED from the edge. The PSNs formed *via* the route shown in (c) efficiently scatter out the in-coupled light, revealing the bee logo. (e) Photograph of the same IJP bee logo on a flexible plastic foil made of polyethylene terephthalate. (f) Representative SEM top-view image of the disordered and uniformly distributed nanoholes (NHs) in a PMMA matrix, fabricated on a glass substrate after selective development of the phase-separated PS domains.

nanostructures over a predefined macroscopic design without the need for additional masks and patterning steps. In addition, the ability to control the precise placement of PSNs on a substrate will provide a means to replicate the physicochemical functions of biological surfaces.<sup>12</sup> The previously reported deposition methods (used for the applications gathered in Table 1) restricted the incorporation of PSNs into uniform films and hence only offered a limited control over the location, size, or geometry of the patterned areas. Only recently were 1D lamellar photonic crystals successfully printed using the self-assembly of bottlebrush block copolymers.<sup>13</sup>

In the present study, we introduce a versatile deposition method to fabricate 2D planar PSNs *via* the inkjet printing (IJP) of homopolymer blend inks, whose formulation can be easily adjusted to fine-tune the phase-separated nanodomains. IJP is particularly attractive for industrial manufacturing owing to its flexibility in the 2D designs to be printed, its high scalability, and its cost-effectiveness.<sup>36</sup> Its benefits are therefore aligned with those provided by a phase-separation process. In what follows, we use a binary blend ink and investigate comprehensively the factors that determine the resulting morphology of the PSNs. We further demonstrate how printed PSNs improve light management in photonic devices, by using them either as light extraction layers for organic light-emitting diodes (OLEDs) or in plasmonic metasurface assays for multiplexed biosensors.

## RESULTS AND DISCUSSION

**Direct Writing of PSNs Enabled by IJP.** The working principle of IJP for the writing of customizable 2D designs incorporating PSNs is schematized in Figure 1a–c. To illustrate how an ink can be formulated for that purpose, we investigated the phase morphology of IJP polymer blend layers based on polystyrene (PS) and poly(methyl methacrylate) (PMMA). After the PS/PMMA blend ink is filled into the IJP nozzle, a waveform applied to a piezoelectric transducer controls the ejection of individual ink droplets in drop-on-demand manner onto the printing substrate to produce the computer defined layout incorporating the PSNs, without template or mask. The rheological properties of the ink, namely its viscosity ( $\eta$ ) and its surface tension ( $\gamma$ ), were tailored before printing to fall into the desired processing window ( $1 < \eta < 25$  mPa·s and  $20 < \gamma < 90$  mN·m<sup>-1</sup>).<sup>37</sup> This was achieved by properly selecting the solvent and the molecular weight of the polymers to reach a stable drop-on-demand printing process. Compared to the well-established spin-coated polymer blend inks,<sup>38</sup> IJP inks are commonly prepared with solvents possessing a boiling point over 150 °C. This helps keep the nozzles wet, therefore avoiding detrimental clogging effects. In this study, inks based on cyclohexanone with or without the cosolvent 1,2,3,4-tetrahydronaphthalene (hereafter referred to by its trade name “Tetralin”) were formulated. In addition, we employed small molecular weight (MW) PS (MW = 19 kg·mol<sup>-1</sup>) and PMMA (MW = 15 kg·mol<sup>-1</sup>) polymers with a concentration of 50 mg·mL<sup>-1</sup> to maintain a stable jetting process. The IJP polymer blend inks

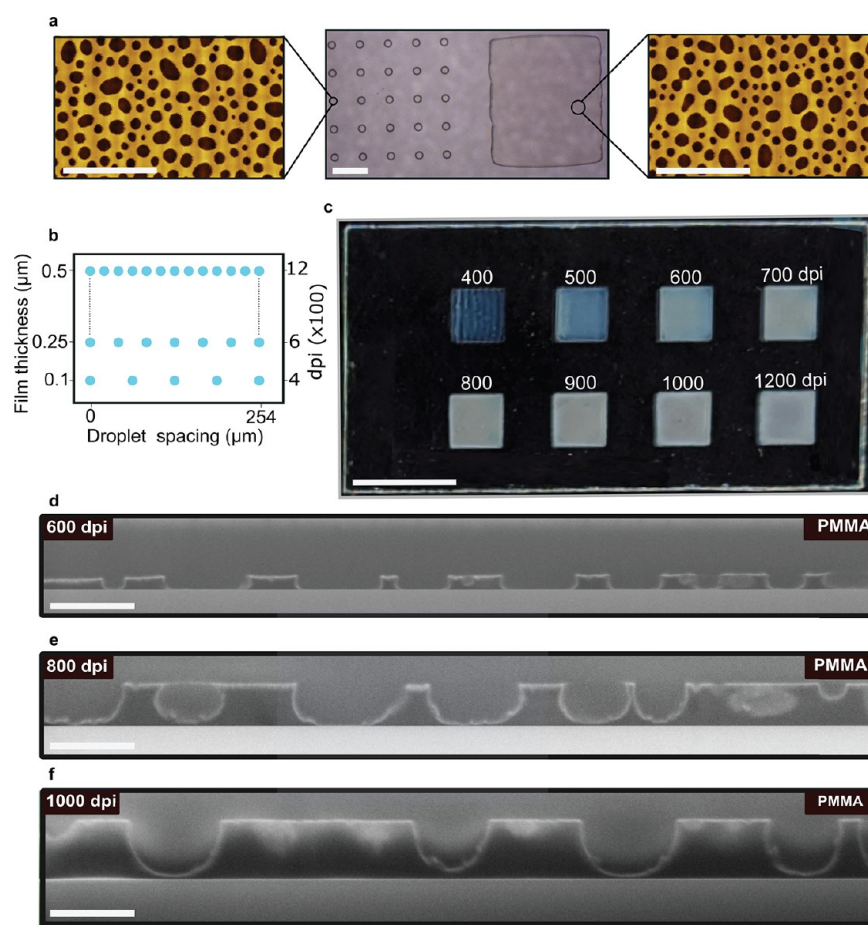


**Figure 2.** Influence of the printed pixel scales and thickness on the nanoscale morphology of the phase-separated polymer films. (a) Light microscopic images of printed pixels with the same thickness but with different lateral scales. The inset AFM images show the corresponding surface morphology. The scale bar in the main and the inset image represents 0.5 mm and 1  $\mu\text{m}$ , respectively. (b) Schematic illustration of film thickness and dpi. (c) Photograph of pixels printed at an increasing resolution and including NHs in a PMMA matrix after selective development of the PS phase (ink based on PS/PMMA (30:70)). The scale bar represents 1 cm. Cross-sectional SEM of pixels printed with a resolution of (d) 600 dpi, (e) 800 dpi, and (f) 1000 dpi. The scale bar represents 0.5  $\mu\text{m}$ .

used are homogeneous at a macroscopic level (see [Supplementary Figure S1](#)) and a single phase exists, while at high concentration of the polymers in the blend the phase-separation might start prior to IJP as reported in other studies based on drop and spin-casting.<sup>38–40</sup> The phase-separation in thin polymer films, however, is fairly different from that in the ink. In thin films, phase-separation is complicated by the presence of the substrate/film and film/air interfaces, giving rise to complex structures.<sup>38,41</sup>

For inks with a weight ratio of PS/PMMA (30:70) in a cosolvent mixture (*i.e.*, cyclohexanone and tetralin in 90:10 volume ratio), PSNs are directly formed and visible after printing upon solvent evaporation at room temperature (see [Figure 1b](#)). A photograph of such a printed film together with its corresponding atomic force microscopy (AFM) image of the PSNs are given as an illustration in [Supplementary Figures S2 and S3](#). The resulting films are nonuniform as schematized in [Figure 1b](#) because of the drying time difference between the printed lines in the direction orthogonal to the printer head movement. This affected the wetting of the ink within the film area. Consequently, they cannot be directly used for most of the applications highlighted in [Table 1](#). One way to improve the film uniformity while preserving the same ink formulation is to increase the number of nozzles used, which was limited to

16 in the present case. Alternatively, one can adapt the ink formulation. Thus, by excluding tetralin as a cosolvent for the PS/PMMA blend, a much better film uniformity was achieved as shown in the photograph of the printed lines forming the bee logo layout (see [Figure 1d,e](#)). The homogeneous hues over the printed bee layout confirm that the printed PSNs are uniformly distributed over a few  $\text{cm}^2$ . The corresponding SEM ([Figure 1f](#)) image shows that the PSNs do not feature local clustering of the phase-separated nanodomains. For this ink formulation, phase separation was assisted by a rapid thermal annealing process after printing (see [Supplementary Figure S4](#)). Initially, the PS/PMMA blend phase forms interface layers at the air–polymer and substrate (wetting layer). In polymer blends, the air–polymer interfacial region is normally enriched in the polymer of lowest surface energy in order to minimize the interfacial free energy.<sup>41,42</sup> Here, despite similar surface energies of PS and PMMA,<sup>41,42</sup> cross-sectional SEM images of focused-ion-beam (FIB) cut PS/PMMA films have demonstrated the tendency of PMMA to form the wetting layer (see [Figure 2](#)). Hence, the only possible reason for the preferential surface enrichment is the influence of the substrate used. The more polar PMMA is strongly attracted to the argon plasma treated substrate, which is hydrophilic. Hence, a wetting layer is formed. After solvent evaporation, the film is annealed on a

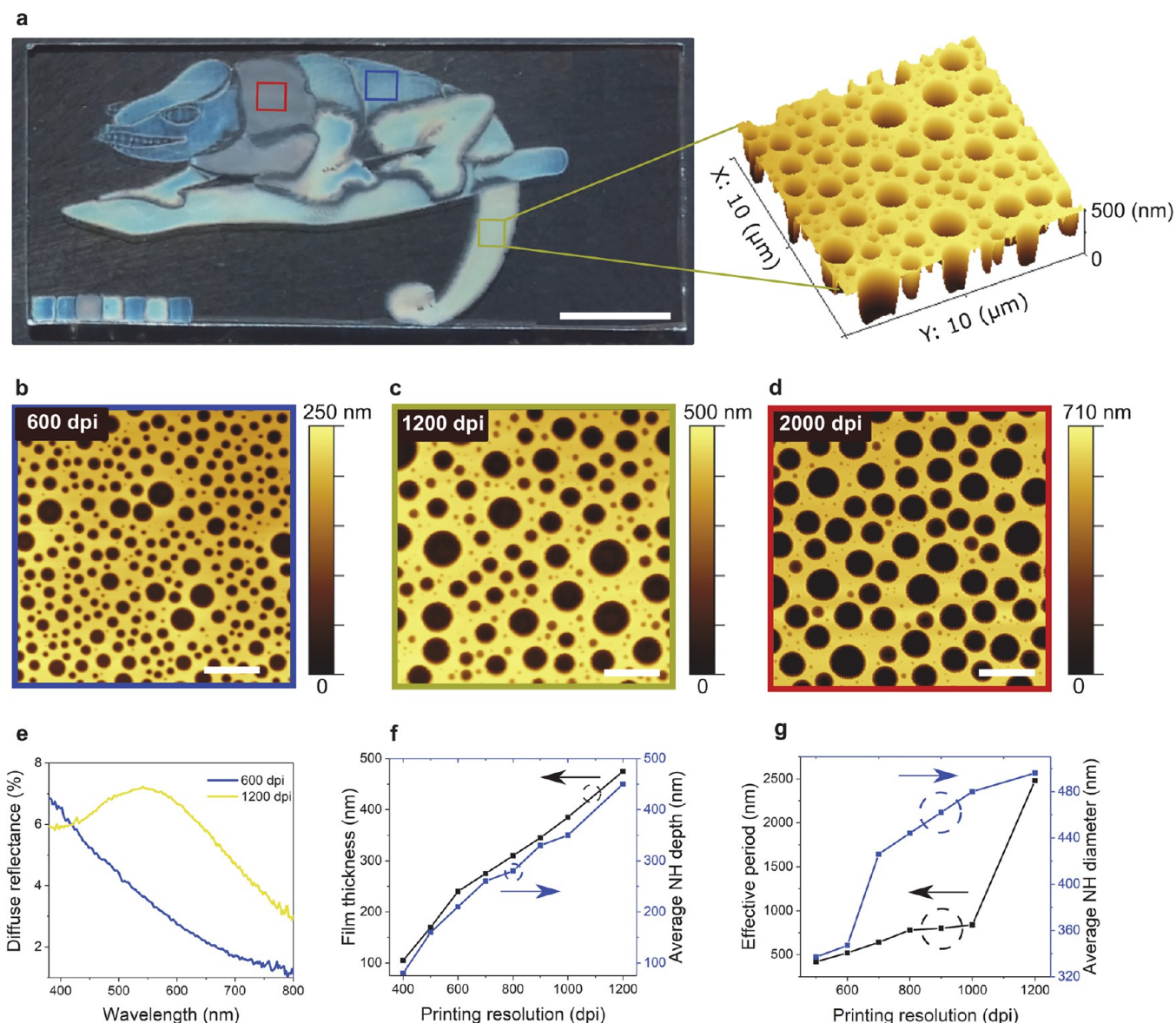


**Figure 3.** Defining the PSN's morphology at the inkjet printing step. (a) Photograph of chameleon logo layout printed with different resolutions and including NHs in a PMMA matrix after selective development of the PS phase (ink based on PS/PMMA (30:70)). The scale bar represents 1 cm. The inset 3D AFM image shows the NHs fabricated with 1200 dpi. (b–d) Corresponding AFM images from selected pixels showing an increase of the mean NH diameter together with the printing resolution. The scale bar represents 2 μm. (e) Measured diffuse reflectance from pixels printed with different dpi over the visible spectrum (under close to normal incidence). (f) Thickness of printed square films (area of 4 mm<sup>2</sup>) measured using contact profilometer before annealing as a function of the printing resolution and average depth of NHs in the PMMA matrix from AFM measurements. Dependence of the PSNs structural parameters as a function of the printing resolution: (g) Effective period of the NH array calculated using a pair correlation function and average diameter of the NHs in the PMMA matrix.

hot plate for 5 min at 150 °C, a temperature higher than the glass transition temperature of both polymers (105 °C for PS and 115 °C for PMMA) under normal atmosphere. Then the phase separation takes place and is either based on nucleation and growth or spinodal decomposition mechanism as schematized in the [Supplementary Figure S5](#).<sup>43</sup> Spinodal decomposition is favored when a homogeneous phase becomes thermodynamically unstable, while for metastable systems the mechanism of nucleation and growth is expected to govern the process.<sup>44,45</sup> Herein, nucleation gives rise to a dispersion of PS rich phase of the minor component as round droplets in the major component PMMA matrix (see [Figure 1f](#)). In contrast, spinodal decomposition leads to disordered bicontinuous

network (tortuous channels); for more details, see the section titled “Temperature and ink composition dependence of the PSN's morphology”. Afterward, one of the two phases is selectively developed as described in the [Experimental Section](#). Although demonstrated with a PS/PMMA blend, our approach can be extended to other binary polymer blends and is applicable to a variety of substrates, be it a rigid glass substrate ([Figure 1d](#)), silicon wafer ([Supplementary Figure S6](#)), or even a flexible plastic foil ([Figure 1e](#)).

In this study, we investigated the dependence of the surface morphology on the printed pixels area. [Figure 2a](#) show examples of pixels printed over a microscopic or a macroscopic scale, including the smallest possible side dimension of 100

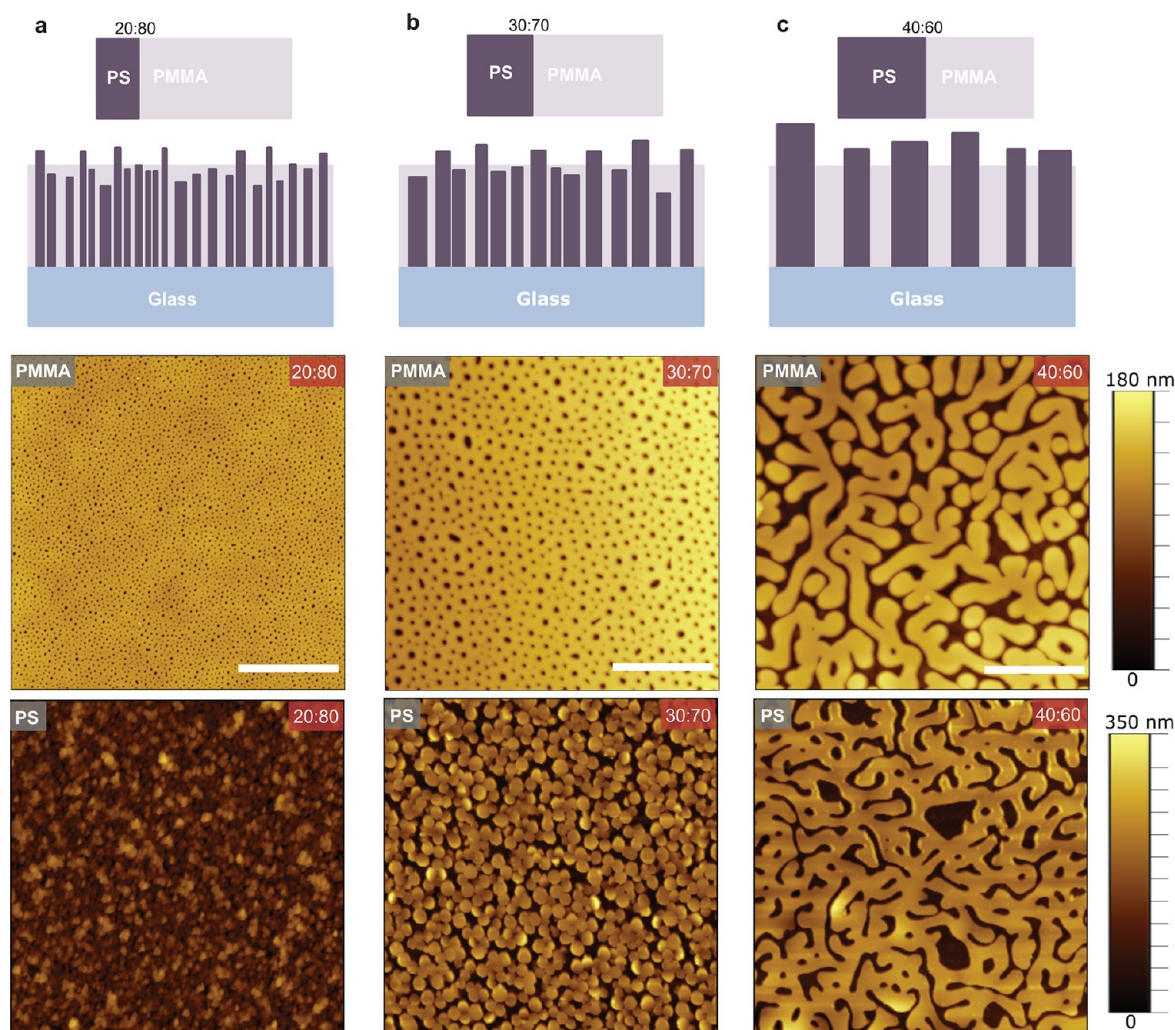


**Figure 4.** Influence of the polymer blend weight ratio on the resulting morphology of the phase-separated nano/micro-domains. Schematics depicting the phase-separation mechanism for different weight ratio. AFM images of the PMMA matrix fabricated using three different PS/PMMA weight ratios (PS/PMMA) = 20:80 (a), 30:70 (b), 40:60 (c), and obtained after 5 min of annealing at 150 °C and after the selective development of the PS phase (middle row) and the PMMA phase (bottom row). The scale bar represents 3  $\mu\text{m}$  in all AFM images.

$\mu\text{m}$ . Printed films with the same thickness shown in Figure 2a on a microscopic and macroscopic scale exhibit similar surface morphology as shown in the inset AFM images. In particular, the average NH depth and diameter for the printed pixels with different scales shown in Figure 2a are 80, 79, 96.2, and 97.4 nm, respectively.

**Dynamic Variation of the PSN's Morphology during Inkjet Printing.** The film thickness is known to be a key parameter for the orientation of the phase-separated domains.<sup>41,46,47</sup> This is attributed to the change in the kinetics of phase-separation<sup>46</sup> and time required for the rearrangement for stable chain conformation depending on the considered film thickness.<sup>41,47</sup> The IJP approach allows controlling the film thickness by simply adapting the printing resolution as schematized in Figure 2b. The relationship between printed PS/PMMA film thickness and dpi follows a linear relationship. Pixels printed over an area of 25 mm<sup>2</sup> with a low resolution (here at 400 dpi) are discontinuous and exhibit a nonuniform film thickness (see Figure 2c). This is expected given the limited number of ink droplets over the printed area. Conversely, continuous films with a uniform thickness can be deposited using a resolution above 500 dpi. Printed pixels

with the same lateral scale but with different film thickness (see Figure 2c) show a significant change in surface morphology. Figure 2d,e shows cross-sectional SEM images of FIB cut pixels printed with different resolutions, and the bright regions in the SEM images are due to the charging effect. For thinner films printed with a resolution <700 dpi, both polymers wet the substrate as shown in Figure 2d and the PS cylinders stand vertically on the substrate (see details in the next section). For thicker films, mainly the PMMA wets the substrate (see Figure 2e,f). The difference of PS phase wetting on the substrate between thick films (no wetting) and thin films (wetting observed) could change the kinetics (mobility) of PS in these films. This might explain the NH size distribution difference between thin and thick printed films.

The capability to tailor the morphology of the IJP phase-separated domains for a given formulation by varying the printing resolution offers an additional benefit on top of the design flexibility shown in Figure 1d,e when compared to the conventional deposition method. From an application viewpoint, it allows us digitally control the in-plane shape, the effective period, and the diameter size distribution of the PSNs at predetermined locations over the same substrate, which

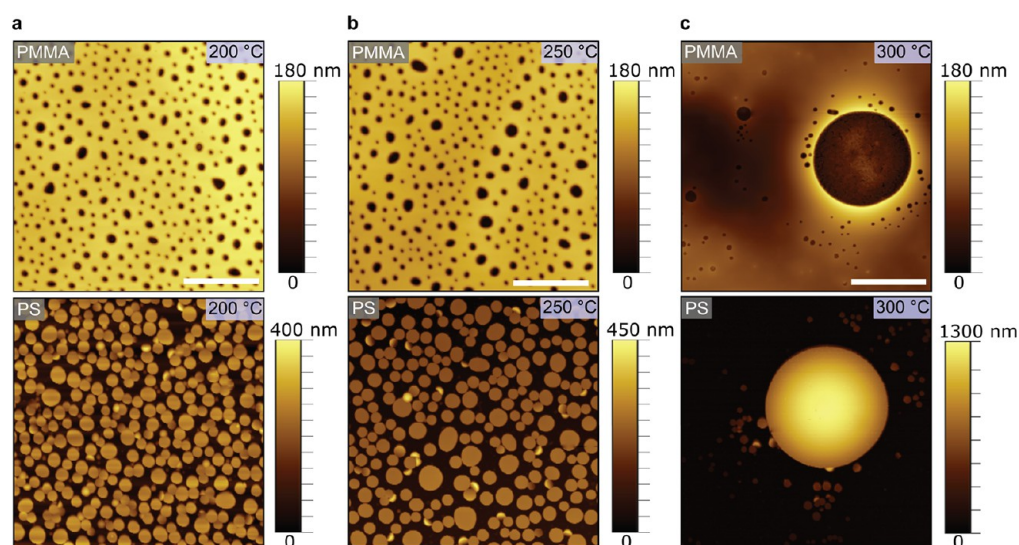


**Figure 5.** Influence of the annealing temperature on the resulting morphology of the phase-separated nano/micro-domains. The AFM images of samples obtained after annealing PS/PMMA (30:70) blend thin films fabricated using 550 dpi at a temperature of 200, 250, and 300 °C for 5 min are shown in (a), (b), and (c), respectively, after selective development of PS (top row) or of PMMA (bottom row). The scale bar in (a) and (b) represents 3 and 9  $\mu\text{m}$  in (c).

would not be possible with ordinary spin-casting approaches.<sup>38</sup> Using the latter, only PSNs with the same morphology across the entire area of the substrate can be processed. In contrast, IJP enables to locally tune the thickness of the printed thin films by changing the resolution and thus the amount of locally deposited ink. As an example, Figure 3a displays the photograph of chameleon logo pixels obtained upon a gradual change of the printing resolution, and after annealing the thin films at 200 °C for 5 min. Figure 3b–d shows the corresponding AFM topography images of the PSNs. The pixels display different haze and colors arising from spectrally dependent light scattering (see Figure 3e) at the PSNs with different feature sizes. The thickness of the printed films (before annealing) reported in Figure 3f increases with the printing resolution. After annealing the films, it is observed that the average diameter and depth of NHs in the PMMA matrix increase with the printing resolution, as shown in Figure 3f,g. Additional information is deduced from the pair correlation function (denoted "PCF"<sup>48</sup>), which gives the probability of finding the center of a selected NH at a given distance from the center of another NH. The PCF was used to derive the effective period from the AFM images. One concludes from Figure 3g that the calculated effective period also increases with the printing resolution.

**Temperature and Ink Composition Dependence of the PSN's Morphology.** Besides tuning the printing resolution, the ink formulation can also be adapted to achieve the desired morphology of the PSNs over a single substrate, for example, by changing the blend composition as illustrated in Figure 4a–c. In many applications (see Table 1), a good control of the size of the PSNs is of utmost importance. As an example, Supplementary Figure S7 shows that PSNs with a diameter size distribution centered at 113 nm can be obtained by increasing the weight ratio of PS in the PS/PMMA blend to 30:70 from an original composition of 20:80, for which this distribution is peaking at 40 nm only. Since the concentration of the ink was fixed, the increase of the PS to PMMA weight ratio increases the PS concentration, which fosters the coalescence of the PS droplets dispersed in the PMMA matrix

and hence increases the lateral size of the PS nanodomains. When the PS weight ratio exceeds a given value, 30% in the present case, one observes a transition of the PSNs morphology from a "sea–island" configuration to a disordered bicontinuous network, involving domains with a width of a few hundreds of nanometers. A representative AFM image is given in Figure 4c for a blend composition of 40:60. For an annealing temperature of 150 °C, the corresponding PS domains for thinner films printed with a resolution of 550 dpi after selective development of the PMMA phase are also shown in Figure 4a–c. Similar density of PS domains and NHs in the PMMA matrix is expected when only switching the developer solvent. Herein, the density of PS domains is significantly higher than the NHs in the PMMA matrix when the PS/PMMA weight ratio is 20:80 and 30:70. The reduction in the NHs density in the PMMA matrix indicate that most PS domains fail to come into a direct contact with the polymer–air interface and are buried in the PMMA layer as illustrated using the schematics in Figure 4a–c. Thus, upon elevated annealing temperature the PS phases that are in non-equilibrium evolve toward the minimization of the interfacial tension.<sup>49–51</sup> Figure 5a–c reveals the influence of the annealing temperature on the morphology of the PS and PMMA phase-separated domains for a PS/PMMA composition of 30:70. As the lateral size and thickness of the PS domains increase with the annealing temperature, which is named coarsening process,<sup>52</sup> the adjacent PMMA layer becomes thinner with an increase in surface coverage. The growth of the PS domains' lateral size is largely determined by the diffusion rate of the PS in the system, which is known to increase with a rise of the annealing temperature.<sup>51</sup> This PS phase coarsening phenomenon in the PMMA matrix follows the Ostwald ripening mechanism.<sup>52</sup> Additional examples are provided in Supplementary Figure S8 and S9 for a PS/PMMA weight ratio of 20:80 and 40:60, respectively. It is worth mentioning that the disordered bicontinuous network formed by spinodal decomposition (see Figure 4c), when the printed PS/PMMA (40:60) film was annealed at 150 °C, evolves into

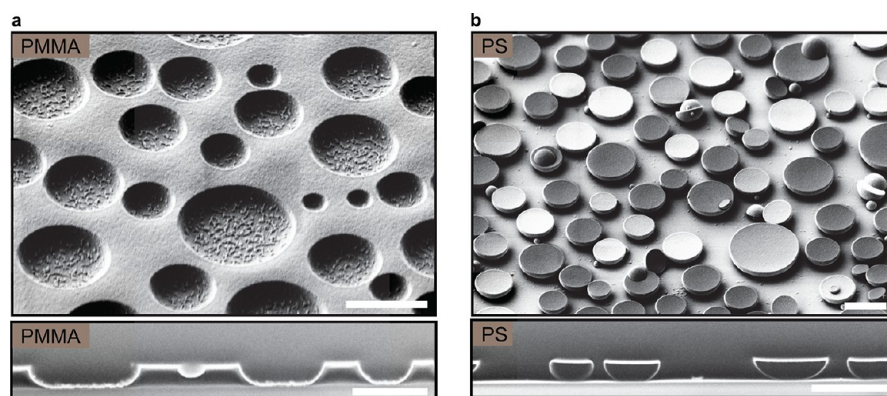


Figure 6. Morphology of the PS domains fabricated with 1000 dpi under a high annealing temperature of 250 °C. SEM top-view images (top row) of 45° tilted samples obtained after annealing PS/PMMA (30:70) blend films and selective development of (a) PS or of (b) PMMA. The bottom row shows the corresponding cross-sectional SEM images of the pixels. The scale bar represents 1  $\mu\text{m}$ .

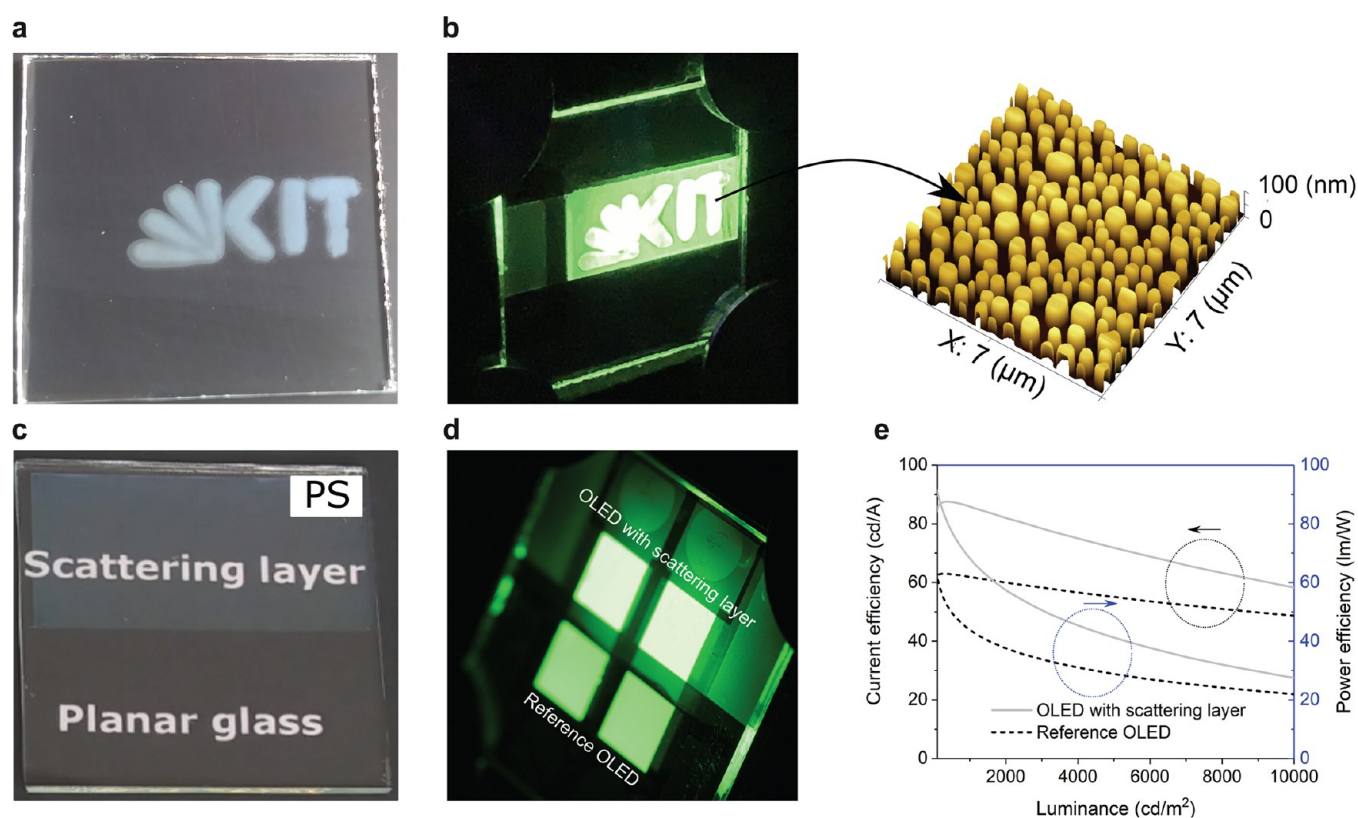
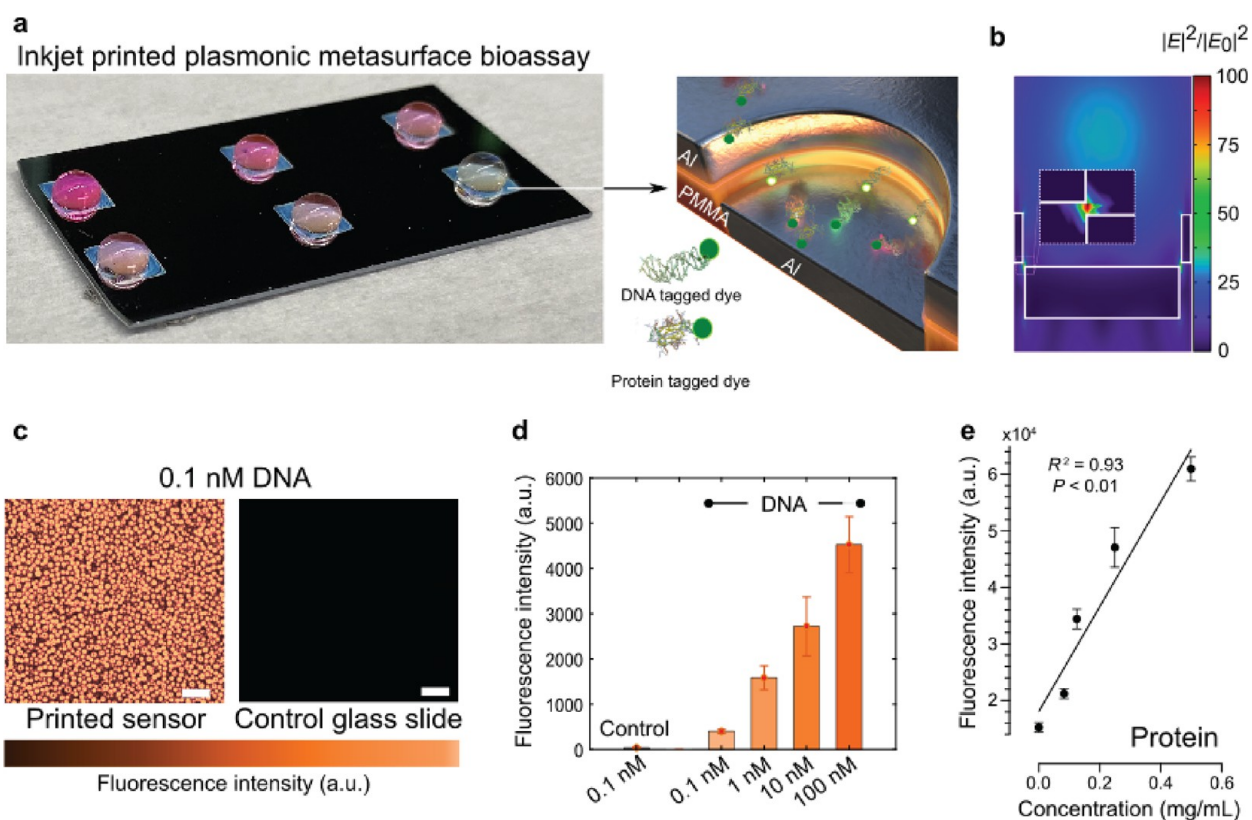


Figure 7. Improved light management in OLEDs processed on top of the IJP compact light extraction layer. (a) Photograph of a printed logo incorporating the PSNs (nanopillars made of PS, average height of 80 nm) after selective development of the PMMA phase, thermal annealing at 200 °C and O<sub>2</sub> plasma treatment. (b) OLED processed on top of the printed glass substrate, emitting more light from the light scattering logo (inset: corresponding light outcoupling nanopillars shown in the 7 × 7  $\mu\text{m}$  AFM image). (c) Glass substrate half-printed with the PSN and (d) resulting bottom-emitting OLED processed atop to quantify the positive impact of the compact light extraction layer on the performance of the light-emitting devices. (e) Current and power efficiency of the OLEDs without (“reference”) and with the printed light scattering layer. The size of all substrates is 25 mm × 25 mm. KIT logo used with permission of the Karlsruhe Institute of Technology.

rounded domains at 300 °C (Figure S9c) in order to minimize the surface energy.<sup>41,42</sup>

In contrast, for thicker printed films (e.g., film prepared using 1000 dpi), at lower temperature (150 °C) the PS domains extend over most of the film thickness but do not reach the interface with the substrate as highlighted in Figure 2f. Here, the selective development of the PMMA layer without removing the PS domains is not possible. With an increase in annealing temperature, the thickness of the PMMA layer

wetting the substrate decreases (see Figure 6a) and the PS domains grow toward the substrate (see Figure 6b). Herein, standing hemispherical PS domains were achieved by selectively developing the PMMA matrix as shown in the cross-sectional SEM images of the FIB cut pixel (Figure 6b). A few PS domains that are not vertically standing on the substrate were also observed as shown in the SEM image of the pixel (see Figure 6b). This is due to the difference in the thickness of the wetting PMMA layer below the PS domains.



**Figure 8.** Printed phase separated self-assemblies based metasurface for POC biosensing (a) Scheme of the biosensing bioassays for protein and DNA detection, fabricated by depositing a thin Al film on top of a PMMA template with NHs to create an array of nanoantennas. The PMMA template is patterned after selective development of PS in the IJP pixels annealed at 200 °C (ink based on PS/PMMA (20:80)). The inset shows an Al nanodisk in a cavity nanoantenna separated with sub-10 nm gap dielectric (PMMA), which acts as an electromagnetic hotspot as well as biomolecule capturing site. (b) Calculated normalized electric field intensity  $\frac{|E|^2}{|E_0|^2}$  at the Cy3 dye excitation peak wavelength ( $\lambda_{\text{peak}} = 555$  nm) of a single nanoantenna with 240 nm in diameter shows a strong field confinement within the 5 nm gap between the disk and cavity. (c) A high-zoomed confocal fluorescence image shows the difference in signal obtained from the printed sensor surface compared to glass control out of 100 pM concentration of Cy3-tagged aptamers. Scale bar: 2  $\mu\text{m}$ . (d) The corresponding enhanced fluorescence signals collected from the printed sensor under varying concentrations down to 100 pM compared to glass control using confocal laser scanning microscope. (e) Detection of protein (streptavidin) on a single-chip printed bioassays with varying concentrations from 0.0 to 0.5  $\text{mg}\cdot\text{mL}^{-1}$  over  $3 \times 3$   $\text{mm}^2$  area with regular low magnification epifluorescence microscope.

The AFM images of the PS domains obtained with an annealing temperature of 200, 250, and 300 °C for 5 min are provided in [Supplementary Figure S10](#). A similar change in the surface morphology of printed PS/PMMA films can be obtained by varying the annealing duration instead of the annealing temperature (see [Supplementary Figure S11](#)). It should be noted that similar PSNs morphologies (and hence optical properties) as highlighted in [Supplementary Figure S12](#) were obtained for samples prepared at different days (for a given ink formulation and for the same printing parameters).

Summing up the results above, the introduced IJP route enables easy adaptation of the morphology of the PSNs at the micro-/nanoscale in pixels shaped according to any predetermined 2D design and printed over the same substrate. This can be achieved by varying the printing resolution, the ink formulation (weight ratio of the binary blends), or the annealing post-treatment. These manifold possibilities facilitate the development of printed photonic layers for various applications, two examples of which are given in the following sections.

**Inkjet Printing of Compact Light Extraction Layers for OLEDs.** OLEDs are gaining increasing market shares for display and lighting applications.<sup>53</sup> However, a notoriously

known limitation hampering this technology is the poor light extraction efficiency in the absence of a proper light management scheme. Taking the example of bottom-emitting OLEDs, only 20–30% of the generated photons are typically outcoupled to the free space.<sup>35,54</sup> Optical loss mechanisms responsible for that effect include light confinement in high refractive index layers (e.g., organic layers, transparent electrodes, and glass substrate),<sup>35,54</sup> as well as the excitation of surface plasmon polaritons at the interface between the metallic electrode and the organic layers.<sup>35,54</sup> To circumvent this issue, light extraction layers based on randomly dispersed or on disordered arrays of light scatterers have been developed to efficiently extract the trapped photons over a broad spectral range.<sup>35,54</sup> In particular, compact light extraction layers that exploit the adjustable light scattering properties of PSNs were processed as a homogeneous and continuous thin film using spin-coating.<sup>35</sup> We here demonstrate that the IJP route allows introducing such a compact light extraction layer into any predetermined 2D design while achieving the targeted light scattering properties for an efficient light outcoupling.

In this study, the printed PSNs are incorporated between the substrate and the OLED thin film stack leading to a nanocorrugation throughout the whole device as illustrated

in the Supplementary Figure S13a. For a corrugated OLED, the height of the printed PSN is the critical parameter to fabricate functional and reproducible devices with improved outcoupling efficiency. Thicker PSN (mean height >150 nm) fabricated with printing resolution >550 dpi led to electrical shorts in the devices. To this end, PSN with a morphology promoting light extraction<sup>35</sup> were formed on a glass substrate by using an ink formulation based on PS/PMMA (30:70) with a printing resolution of 550 dpi. For the selected in-plane configuration, light scattering and optical transmittance were further adjusted to improve the outcoupling efficiency in an OLED by adapting the PSN mean height with O<sub>2</sub> plasma treatment. The optical properties are analyzed in more details in Supplementary Figure S13b,c.

As an example, to highlight the potential of IJP light outcoupling PSN over other techniques,<sup>35</sup> a light scattering layer was printed so as to form the Karlsruhe Institute of Technology logo (see Figure 7a), prior to the deposition of the complete OLED thin film stack atop. Figure 7b allows to qualitatively assess the higher fraction of photons outcoupled from this logo when compared to the surrounding emissive area. To quantify this improvement, additional OLEDs were processed by using only half-printed glass substrates (Figure 7c,d). At a luminance of 1000 cd/m<sup>2</sup>, the power efficiency ( $\eta_p$ ) of the emissive pixels equipped with the PSNs reaches 69 lm/W against only 44 lm/W for an equivalent reference without the printed light scattering layers. The corresponding current efficiency ( $\eta_L$ ) increases to 86 cd/A from its reference value of 62 cd/A. This enhancement notably originates from the efficient light scattering owing to the refractive index ( $n$ ) contrast between the printed PSNs (here based on PS with  $n = 1.6$  at  $\lambda_{\text{peak}} = 520$  nm) and the indium tin oxide anode atop ( $n = 2$  at  $\lambda_{\text{peak}} = 520$  nm). Therefore, internal modes propagating within the organic layers and the transparent conductive oxide anode can be efficiently extracted. Unlike the reference devices, which exhibit strong variations of their emission spectra upon a change of the viewing angle, OLEDs processed on top of the printed PSNs are free from such color distortion effects (see Supplementary Figure S13e,f). Jiao *et al.*<sup>35</sup> also observed a similar behavior using spin-coated PSN. However, the relative  $\eta_p$  and  $\eta_L$  enhancement obtained using IJP PSN is significantly higher than the values reported in ref.<sup>35</sup> It should be noted that the OLED stack used in this study and ref.<sup>35</sup> are different and the spin-coated PSN were integrated in the OLED stack without selective development of the PS or the PMMA phase.

Currently, IJP is receiving an increased attention from OLED-manufacturers as it enables a direct definition of RGB pixels and has the potential to reduce the production costs.<sup>53</sup> In the future, one could therefore combine the IJP of the OLED stack and of a compact light extraction layer for achieving a greater design flexibility, material yield, and light outcoupling efficiency.

#### Inkjet-Printing Enabled Metasurfaces for Biosensing.

We further exemplify the use of printed PSNs for photonic applications by developing low-cost plasmonic metasurface based bioassays for multiplexed point-of-care (POC) biosensing. Designed similar to commercial enzyme-linked immunosorbent assays (ELISA) well-plates,<sup>55</sup> we here demonstrate a 6-well plate scheme, as shown in Figure 8a. We note that our approach can be extended to any number of wells. ELISAs, typically limited to protein sensing, require sophisticated and time-consuming laboratory-grade detection schemes such as plate readers for readout and several hours for sample

preparation. In comparison, fluorescence enhancement rendered by the nanostructured wells allows for rapid biosensing of different biomolecules such as proteins and DNA aptamers on the same platform with high sensitivity using a ubiquitous epifluorescence microscope at low magnification (5 $\times$ ) making this route suitable for limited-resource settings. The sensing wells are formed in a two-step procedure: the printing of the PS/PMMA ink followed by the development of the phase-separated PS nanodomains, and the deposition of a thin aluminum coating on the resulting PMMA template with NH<sub>3</sub>. The wells are therefore comprised of a nanoantenna array composed of Al nanodisks in printed PMMA and Al cavities (Figure 8a). The sub-10 nm gap of PMMA between the Al nanodisk and the cavity forms an electromagnetic ring of hotspot as shown in Figure 8b<sup>23</sup> and allows extremely efficient light transfer between the far- and near-fields using the hybrid multipolar plasmonic modes in the visible spectrum.<sup>30</sup> The use of Al here instead of expensive and conventional plasmonic metals like Au and Ag is an added advantage to produce cost-effective POC biosensors.<sup>56</sup> Moreover, the printed PMMA hotspots work as molecular aggregators in contrast to traditional oxide-based dielectrics to additionally enhance molecular enhancement because of increased affinity of physisorption toward both nucleic acids and proteins.<sup>30</sup>

The multiplex detection of different analytes on the printed sensor was tested using various low-concentration DNA aptamers with varying concentrations down to 100 pM on a single-chip bioassays and compared with reference flat microscopy glass slides to confirm the high detection sensitivity (Figure 8c,d). Figure 8c shows a high-zoomed confocal image of strong fluorescence signal from the 100 pM DNA sample on the printed sensor in comparison to a regular glass slide. Quantitatively, there is over 10-fold fluorescence signal improvement for a very low concentration (100 pM) Cy3 dye tagged DNA aptamers. Similarly, over 10-fold increase of fluorescence signals is observed for change in DNA concentrations from 100 pM to 100 nM with a linear trend demonstrating its potential for biosensing.

Finally, protein sensing was also performed using low magnification (5 $\times$  objective) and a low power LED source to demonstrate the suitability as a low-cost POC biosensor. Various concentrations of streptavidin conjugated with Alexa Fluor 555 (excitation: 555 nm, emission: 580 nm with an intrinsic quantum yield,  $\eta_0 = 0.10$ ) were detected through plasmon-enhanced fluorescence, which yielded spatially uniform signals from over a millimeter-scale distance. Using this scheme, as shown in Figure 8e, concentrations of streptavidin conjugates from 0–0.5 mg·mL<sup>-1</sup> were detected with excellent linearity ( $R^2 = 0.93$ ,  $P < 0.01$ ).

## CONCLUSIONS

In summary, we have demonstrated an elegant way toward digitally printable nanophotonic structures. Our inkjet printing based approach has two key advances: (1) phase-separated domains with a scaling from a few micrometers down to sub-100 nm range, processed on arbitrary substrates and obtained within any predetermined 2D design without template or mask, and (2) two ways of varying the morphology of the phase-separated micro/nanostructures during printing, either by adapting the printing resolution from pixel to pixel for a given ink formulation, or by working with multiple inks (using, for example, different PS/PMMA weight ratios). While this approach was introduced with a homopolymer blend ink, it is

also applicable to block copolymers and biopolymers. Moreover, as this cost-effective method can be readily scaled up to large areas, we anticipate that it will foster the widespread implementation of PSNs in nanophotonic applications. To this end, we have shown that IJP PSNs can serve as compact internal light extraction layers for OLEDs, significantly improving the power and current efficiency with respect to emissive pixels processed on planar substrates ( $\eta_p$  and  $\eta_L$  relative increase of +57% and +39%, respectively). Moreover, we have devised Al-based metasurfaces using IJP PSNs for POC biosensing. The latter utilize hybrid multipolar plasmonic modes and generate a 100-fold enhancement of the near-field and a 5-fold increase in the quantum yield (far-field) of the fluorescent dyes, in addition to 4-fold enhancement of localized molecular aggregation in PMMA hotspots. Our results show the potential functionality of IJP PSNs to develop bioassays similar to commercial enzyme-linked ELISA well-plates with lower-cost and higher speed of analysis. With further improvement in device performance through design and printing optimization, machine learning and software implementation, this technology is envisioned to be integrated into more compact nanophotonic and IoT platforms in future.

## EXPERIMENTAL SECTION

### Inkjet Printing of Phase-Separated Micro-/Nanostructures.

PS and PMMA were purchased from Polymer Standards Service GmbH (PSS). PS/PMMA mixtures with mass ratios of 20:80, 30:70, and 40:60 were prepared and dissolved in cyclohexanone (Alfa Aesar 99%) and tetraline (Sigma-Aldrich 99%) with a concentration of 50 g L<sup>-1</sup>. Prior to printing, the inks were filtered with a 0.2  $\mu\text{m}$  polytetrafluoroethylene filter (Carl Roth GmbH). The substrates based on glass (Schott), silicon (SIEGERT WAFER GmbH), and PET (Putz GmbH + Co. Folien KG) were cleaned in acetone and 2-propanol in an ultrasonic bath for 10 min each, dried with nitrogen, and exposed to argon plasma (Tetra 30, Diener electronics GmbH + Co. KG) for 5 min.

PixDro LP50 (Meyer Burger, Inc.) equipped with a DMC-16110 cartridge (FujiFilm) with a nominal drop volume of 10 pL and a custom-designed waveform was used to deposit the PS/PMMA inks. The print head temperature was set to 30 °C, and the substrate temperature was set to 25 °C. The printing speed was set to 450 mm s<sup>-1</sup>. The structures were printed with 550 dpi resolution with a quality factor of 4. The substrates were annealed at 150 °C for 5 min. After phase-separation of the polymer blends, PS was selectively developed using cyclohexane (Merck KGaA) and PMMA with acetic acid (ThermoFisher GmbH). IJP PS nanopillars used for the fabrication of OLED devices were treated with oxygen plasma (Femto, Diener electronics GmbH + Co. KG) at an operational power of 50 W and the O<sub>2</sub> flow rate was fixed at 45 cm<sup>3</sup> min<sup>-1</sup> (qn). Unless mentioned otherwise, all preparation steps were performed at ambient clean room conditions.

**OLED Fabrication.** Indium tin oxide (ITO) was used as a transparent anode material and processed by a Kurt J Lesker PVD-75 thin film deposition system. The deposition of 135 nm ITO films was carried out onto precleaned planar and IJP PSNs coated glass substrates during 2000 s at room temperature (25 °C), 0.8 mTorr, and 2.5% of O<sub>2</sub> as a reactive gas. The samples were then annealed for 15 min on a hot plate at 200 °C to improve the optical transmission of the ITO films as well as their electrical conductivity (corresponding sheet resistance of 22.9 Ohms/sq). The green-emitting OLED stack's organic layers were deposited using a high vacuum thermal evaporator (Lesker Spectros) at a pressure of 10<sup>-6</sup> mbar. The OLED stack consists of molybdenum oxide (MoO<sub>3</sub>) as a hole injection material, 4,4',4''-tris[phenyl(*m*-tolyl)amino]triphenylamine (*m*-MTDATA) as a hole transport material, and tris[2-phenylpyridinato-C<sub>2</sub>N]iridium(III) (Ir(ppy)<sub>3</sub>) as the emitter material doped in a double-layer consisting of the hole and the electron transport materials both at a

concentration of 7 vol %. As an electron-transport material, we evaporated 4,7-diphenyl-1,10-phenanthroline (BPhen) followed by lithium fluoride (LiF) and aluminum (Al) as the cathode material. The final OLED stack consists of 5 nm MoO<sub>3</sub>, 15 nm *m*-MTDATA, 20 nm *m*-MTDATA:Ir(ppy)<sub>3</sub>, 20 nm BPhen:Ir(ppy)<sub>3</sub>, 40 nm BPhen, 1 nm LiF, and 100 nm Al.

**Simulation and Fabrication of IJP Aluminum Metasurface Based Bioassays.** 3D optical simulations of a single nanoantenna for calculating the field intensity and quantum yield enhancements were set up in the FDTD Maxwellian solver Lumerical 2019a. Three nm of native alumina is considered on top of Al nanostructures for all simulations. E-field were calculated using TFSF plane wave illumination at normal incidence. Local density of states simulations of a dipole due to nanoantenna were performed using Green's function analysis in Lumerical to calculate quantum yield enhancements.

The printed bioassays were fabricated by evaporating a thin film Al of 140 nm using Lesker labline e-beam evaporator (Kurt J. Lesker, USA) at a rate of 1 Å/s and a pressure of 3 × 10<sup>-8</sup> Torr on a 150 nm thick printed PMMA nanoholes. The measured nanogap of the final plasmonic metasurfaces was found to be 5.89 ± 1.63 nm ( $n = 40$ ).

**Topographical Investigation.** The investigated samples' morphology was probed using a JPK nanoWizard II atomic force microscope in intermittent contact mode under ambient conditions. The top view image was acquired using scanning electron microscopy (SUPRA 60 VP, Carl Zeiss Microscopy GmbH, Germany); the sample was coated with a thin gold layer using JFC-1200 fine coater (JEOL) beforehand.

**Optical Characterization.** The printed films' optical characteristics were extracted from transmittance and reflectance data, measured using a UV-vis spectrometer (Lambda 1050, PerkinElmer, Inc.) equipped with a 150 mm integrating sphere. The diffused reflectance and transmittance were performed by letting the direct reflectance and transmittance escape from the integrating sphere.

**OLED Characterization.** The fabricated OLEDs' electrical characteristics were measured using a source measurement unit (Keithley 2400), their luminous flux was determined by an integrating sphere attached to a spectrometer (Instrument Systems CAS140), and their current efficiencies were determined assuming a Lambertian emission. The OLED measurements were done in a nitrogen atmosphere to avoid degradation of the device. The angular emission profile was measured using a spectrometer (Ocean Optics USB2000+) pointing toward the OLED device, which was mounted on a rotating stage. The substrate mode emission was blocked by covering the OLED device's edges with a black film layer.

**Characterization of the Printed Aluminum Metasurface Based Bioassays.** Single-stranded DNA or aptamers (Integrated DNA Technologies, USA) in Tris-HCl buffer (pH 7.4) were added (drops of 30  $\mu\text{L}$  of different concentrations) to the printed wells and covered by coverslips for 30 min incubation at room temperature. The aptamer was labeled with Cy3 dye at the 5' end, and a spacer sequence was placed between the dye and rest of the DNA sequence to allow proper folding. The custom aptamer sequence: 5'-Cy3-/A/iSP9/-GGTGGTGGGGGGGGTTGGTAGGG TGTCTTC-3'. Fluorescence images were obtained using an inverted Zeiss confocal laser scanning microscope (LSM 800, Carl Zeiss AG, Germany) with a 100X, oil immersion objective (NA: 1.46) under laser excitation power of 4  $\mu\text{W}$ .

Streptavidin conjugates (ThermoFisher Scientific, USA) of various concentrations between 0 and 0.5 mg mL<sup>-1</sup> in phosphate-buffered saline were added (drops of 30  $\mu\text{L}$ ) to the printed sensor for a 1 h incubation at room temperature. Following this, the sensor was washed gently in DI water for 30 min and prepared for detection. Fluorescence imaging was conducted using a Leica DMI 600 wide field microscope (Leica Camera AG, Germany) with a 5X objective in conjunction with a Lumencor SPECTRA X (Lumencor, Inc., USA) illumination system.

ImageJ (National Institutes of Health, USA), a public-domain and Java-based image processing tool, was used to obtain fluorescence intensity from regions of interest (ROIs). The fluorescence intensity

was computed as a means to measure the intensity of each constituent pixel in the ROI.

## ASSOCIATED CONTENT

### Supporting Information

The Supporting Information is available free of charge at <https://pubs.acs.org/doi/10.1021/acsnano.1c00552>.

Detailed discussion about a phase separation in polymer blend inks, the phase diagram of a polymer blend of PS and PMMA, inkjet printing of PSNs on silicon substrates, inkjet printing of PSNs at room temperature, the influence of the polymer blend composition on the resulting PSNs diameter size distribution, the influence of the annealing temperature on the morphology of the printed PSNs, and inkjet printing of compact light extraction layers for OLEDs (PDF)

## AUTHOR INFORMATION

### Corresponding Authors

**Yidnekachew J. Donie** – Light Technology Institute, Karlsruhe Institute of Technology, 76131 Karlsruhe, Germany; [orcid.org/0000-0003-1204-1427](https://orcid.org/0000-0003-1204-1427); Email: [yidnekachew.donie@kit.edu](mailto:yidnekachew.donie@kit.edu)

**Uli Lemmer** – Light Technology Institute, Karlsruhe Institute of Technology, 76131 Karlsruhe, Germany; InnovationLab, 69115 Heidelberg, Germany; Institute of Microstructure Technology, Karlsruhe Institute of Technology, 76344 Eggenstein-Leopoldshafen, Germany; [orcid.org/0000-0001-9892-329X](https://orcid.org/0000-0001-9892-329X); Email: [ulrich.lemmer@kit.edu](mailto:ulrich.lemmer@kit.edu)

**Guillaume Gomard** – Light Technology Institute, Karlsruhe Institute of Technology, 76131 Karlsruhe, Germany; Institute of Microstructure Technology, Karlsruhe Institute of Technology, 76344 Eggenstein-Leopoldshafen, Germany; Email: [guillaume.gomard@zeiss.com](mailto:guillaume.gomard@zeiss.com)

### Authors

**Stefan Schliske** – Light Technology Institute, Karlsruhe Institute of Technology, 76131 Karlsruhe, Germany; InnovationLab, 69115 Heidelberg, Germany; [orcid.org/0000-0002-3220-8012](https://orcid.org/0000-0002-3220-8012)

**Radwanul H. Siddique** – Image Sensor Lab, Samsung Semiconductor, Inc., Pasadena, California 91101, United States; Medical Engineering, California Institute of Technology (Caltech), Pasadena, California 91125, United States; [orcid.org/0000-0001-7494-5857](https://orcid.org/0000-0001-7494-5857)

**Adrian Mertens** – Light Technology Institute, Karlsruhe Institute of Technology, 76131 Karlsruhe, Germany; Institute of Microstructure Technology, Karlsruhe Institute of Technology, 76344 Eggenstein-Leopoldshafen, Germany

**Vinayak Narasimhan** – Medical Engineering, California Institute of Technology (Caltech), Pasadena, California 91125, United States; [orcid.org/0000-0003-4165-402X](https://orcid.org/0000-0003-4165-402X)

**Fabian Schackmar** – Light Technology Institute, Karlsruhe Institute of Technology, 76131 Karlsruhe, Germany; InnovationLab, 69115 Heidelberg, Germany; Institute of Microstructure Technology, Karlsruhe Institute of Technology, 76344 Eggenstein-Leopoldshafen, Germany

**Manuel Pietsch** – Light Technology Institute, Karlsruhe Institute of Technology, 76131 Karlsruhe, Germany; InnovationLab, 69115 Heidelberg, Germany

**Ihtezaz M. Hossain** – Light Technology Institute, Karlsruhe Institute of Technology, 76131 Karlsruhe, Germany; Institute of Microstructure Technology, Karlsruhe Institute of

Technology, 76344 Eggenstein-Leopoldshafen, Germany;

[orcid.org/0000-0001-6533-1757](https://orcid.org/0000-0001-6533-1757)

**Gerardo Hernandez-Sosa** – Light Technology Institute, Karlsruhe Institute of Technology, 76131 Karlsruhe, Germany; InnovationLab, 69115 Heidelberg, Germany;

[orcid.org/0000-0002-2871-6401](https://orcid.org/0000-0002-2871-6401)

Complete contact information is available at:

<https://pubs.acs.org/doi/10.1021/acsnano.1c00552>

### Author Contributions

Y.J.D., S.S., and G.G. conceived the study. Y.J.D., R.H.S., and G.G. designed the analyses. Y.J.D., S.S., A.M., F.S., and M.P. optimized IJP ink formulation and fabricated the samples with IJP PSNs. Y.J.D. conducted the microscopy and optical characterization of the samples. Y.J.D. and I.M.H. conducted the optimization and deposition of the ITO for OLED devices. Y.J.D. fabricated and characterized the OLED devices. R.H.S. and V.N. conducted the simulation, fabrication, and characterization of the biosensor devices. G.G., G.H.S., and U.L. supervised the project. Y.J.D., R.H.S., U.L., and G.G. wrote the initial manuscript. All authors discussed the results and commented on the manuscript.

### Notes

The authors declare no competing financial interest.

### ACKNOWLEDGMENTS

Y.J.D. is part of the Max Planck School of Photonics supported by BMBF, Max Planck Society, and Fraunhofer Society. The KIT team gratefully acknowledges support from the Karlsruhe School of Optics & Photonics ([www.ksop.de](http://www.ksop.de)). The KIT team also acknowledges funding by the Deutsche Forschungsgemeinschaft (DFG, German Research Foundation) under Germany's Excellence Strategy via the Excellence Cluster 3D Matter Made to Order (Grant No. EXC-2082/1-390761711). R.H.S. and V.N. gratefully acknowledge critical support and infrastructure provided for this work by the Kavli Nanoscience Institute, Caltech Beckman Institute, and the Arnold and Mabel Beckman Foundation at Caltech and Samsung Global Research Outreach program.

### REFERENCES

- (1) Reich, S.; Cohen, Y. Phase Separation of Polymer Blends in Thin Films. *J. Polym. Sci., Polym. Phys. Ed.* **1981**, *19*, 1255–1267.
- (2) Karim, A.; Slawacki, T. M.; Kumar, S.; Douglas, J.; Satija, S.; Han, C.; Russell, T.; Liu, Y.; Overney, R.; Sokolov, J.; Rafailovich, M. Phase-Separation-Induced Surface Patterns in Thin Polymer Blend Films. *Macromolecules* **1998**, *31*, 857–862.
- (3) Jeon, K. W.; Walter, H.; Brooks, D. E.; Srere, P. A. *Microcompartmentation and Phase Separation in Cytoplasm: A Survey of Cell Biology*, 1st ed.; Academic Press: San Diego, 1999; Vol. 192, pp 3–175.
- (4) Burg, S. L.; Parnell, A. J. Self-Assembling Structural Colour in Nature. *J. Phys.: Condens. Matter* **2018**, *30*, 413001.
- (5) Dufresne, E. R.; Noh, H.; Saranathan, V.; Mochrie, S. G.; Cao, H.; Prum, R. O. Self-Assembly of Amorphous Biophotonic Nanostructures by Phase Separation. *Soft Matter* **2009**, *5*, 1792–1795.
- (6) Fan, T.; Yu, X.; Shen, B.; Sun, L. Peptide Self-Assembled Nanostructures for Drug Delivery Applications. *J. Nanomater.* **2017**, 1–16.
- (7) Meredith, J. C.; Amis, E. J. LCST Phase Separation in Biodegradable Polymer Blends: Poly (D, L-Lactide) and Poly (-Caprolactone). *Macromol. Chem. Phys.* **2000**, *201*, 733–739.

- (8) Strobel, N.; Eckstein, R.; Lehr, J.; Lemmer, U.; Hernandez-Sosa, G. Semiconductor: Insulator Blends for Speed Enhancement in Organic Photodiodes. *Adv. Electron. Mater.* **2018**, *4*, 1700345.
- (9) Chen, Z.; Wang, X.; Qi, Y.; Yang, S.; Soares, J. A.; Apgar, B. A.; Gao, R.; Xu, R.; Lee, Y.; Zhang, X.; Yao, J.; Martin, L. W. Self-Assembled, Nanostructured, Tunable Metamaterials via Spinodal Decomposition. *ACS Nano* **2016**, *10*, 10237–10244.
- (10) Tseng, Y.-C.; Darling, S. B. Block Copolymer Nanostructures for Technology. *Polymers* **2010**, *2*, 470–489.
- (11) Black, C. T.; Ruiz, R.; Breyta, G.; Cheng, J. Y.; Colburn, M. E.; Guarini, K. W.; Kim, H.-C.; Zhang, Y. Polymer Self Assembly in Semiconductor Microelectronics. *IBM J. Res. Dev.* **2007**, *51*, 605–633.
- (12) Calvert, P. Printing Cells. *Science* **2007**, *318*, 208–209.
- (13) Patel, B. B.; Walsh, D. J.; Kim, D. H.; Kwok, J.; Lee, B.; Guirounet, D.; Diao, Y. Tunable Structural Color of Bottlebrush Block Copolymers through Direct-Write 3D Printing from Solution. *Sci. Adv.* **2020**, *6*, No. eaaz7202.
- (14) Ruiz, R.; Kang, H.; Detcheverry, F. A.; Dobisz, E.; Kercher, D. S.; Albrecht, T. R.; de Pablo, J. J.; Nealey, P. F. Density Multiplication and Improved Lithography by Directed Block Copolymer Assembly. *Science* **2008**, *321*, 936–939.
- (15) Yang, X.; Wan, L.; Xiao, S.; Xu, Y.; Weller, D. K. Directed Block Copolymer Assembly versus Electron Beam Lithography for Bit-Patterned Media with Areal Density of 1 Terabit/Inch<sup>2</sup> and Beyond. *ACS Nano* **2009**, *3*, 1844–1858.
- (16) Black, C. Self-Aligned Self Assembly of Multi-Nanowire Silicon Field Effect Transistors. *Appl. Phys. Lett.* **2005**, *87*, 163116.
- (17) Tsai, H.; Pitera, J. W.; Miyazoe, H.; Bangsaruntip, S.; Engelmann, S. U.; Liu, C.-C.; Cheng, J. Y.; Bucchignano, J. J.; Klaus, D. P.; Joseph, E. A.; Sanders, D. P.; Colburn, M. E.; Guillorn, M. A. Two-Dimensional Pattern Formation Using Graphoepitaxy of PS-b-PMMA Block Copolymers for Advanced FinFET Device and Circuit Fabrication. *ACS Nano* **2014**, *8*, 5227–5232.
- (18) Park, W. I.; You, B. K.; Mun, B. H.; Seo, H. K.; Lee, J. Y.; Hosaka, S.; Yin, Y.; Ross, C.; Lee, K. J.; Jung, Y. S. Self-Assembled Incorporation of Modulated Block Copolymer Nanostructures in Phase-Change Memory for Switching Power Reduction. *ACS Nano* **2013**, *7*, 2651–2658.
- (19) Guarini, K.; Black, C.; Zhang, Y.; Babich, I.; Sikorski, E.; Gignac, L. Low Voltage, Scalable Nanocrystal FLASH Memory Fabricated by Templated Self Assembly. *IEEE* **2003**, 22–2.
- (20) Kim, H.; Wei, W.; Kuech, T. F.; Gopalan, P.; Mawst, L. J. Impact of InGaAs Carrier Collection Quantum Well on the Performance of InAs QD Active Region Lasers Fabricated by Diblock Copolymer Lithography and Selective Area Epitaxy. *Semicond. Sci. Technol.* **2019**, *34*, 025012.
- (21) Black, C. T.; Guarini, K. W.; Zhang, Y.; Kim, H.; Benedict, J.; Sikorski, E.; Babich, I. V.; Milkove, K. R. High-Capacity, Self-Assembled Metal-Oxide-Semiconductor Decoupling Capacitors. *IEEE Electron Device Lett.* **2004**, *25*, 622–624.
- (22) Kim, J. Y.; Kim, H.; Kim, B. H.; Chang, T.; Lim, J.; Jin, H. M.; Mun, J. H.; Choi, Y. J.; Chung, K.; Shin, J.; Fan, S.; Kim, S. O. Highly Tunable Refractive Index Visible-Light Metasurface from Block Copolymer Self-Assembly. *Nat. Commun.* **2016**, *7*, 1–9.
- (23) Siddique, R. H.; Mertens, J.; Hölscher, H.; Vignolini, S. Scalable and Controlled Self-Assembly of Aluminum-Based Random Plasmonic Metasurfaces. *Light: Sci. Appl.* **2017**, *6*, e17015–e17015.
- (24) Joo, W.; Park, M. S.; Kim, J. K. Block Copolymer Film with Sponge-Like Nanoporous Structure for Antireflection Coating. *Langmuir* **2006**, *22*, 7960–7963.
- (25) Walheim, S.; Schäffer, E.; Mlynek, J.; Steiner, U. Nanophase-Separated Polymer Films as High-Performance Antireflection Coatings. *Science* **1999**, *283*, 520–522.
- (26) Kang, Y.; Walish, J. J.; Gorishnyy, T.; Thomas, E. L. Broad-Wavelength-Range Chemically Tunable Block-Copolymer Photonic Gels. *Nat. Mater.* **2007**, *6*, 957–960.
- (27) Chan, E. P.; Walish, J. J.; Thomas, E. L.; Stafford, C. M. Block Copolymer Photonic Gel for Mechanochromic Sensing. *Adv. Mater.* **2011**, *23*, 4702–4706.
- (28) Meier, T.; Solares, S. D. Rhodamine-Doped Nanoporous Polymer Films as High-Performance Anti-Reflection Coatings and Optical Filters. *Nanoscale* **2016**, *8*, 17675–17685.
- (29) Narasimhan, V.; Siddique, R. H.; Lee, J. O.; Kumar, S.; Ndjamien, B.; Du, J.; Hong, N.; Sretavan, D.; Choo, H. Multifunctional Biophotonic Nanostructures Inspired by the Longtail Glasswing Butterfly for Medical Devices. *Nat. Nanotechnol.* **2018**, *13*, 512–519.
- (30) Siddique, R. H.; Kumar, S.; Narasimhan, V.; Kwon, H.; Choo, H. Aluminum Metasurface with Hybrid Multipolar Plasmons for 1000-Fold Broadband Visible Fluorescence Enhancement and Multiplexed Biosensing. *ACS Nano* **2019**, *13*, 13775–13783.
- (31) Narasimhan, V.; Siddique, R. H.; Hoffmann, M.; Kumar, S.; Choo, H. Enhanced Broadband Fluorescence Detection of Nucleic Acids Using Multipolar Gap-Plasmons on Biomimetic Au Metasurfaces. *Nanoscale* **2019**, *11*, 13750–13757.
- (32) Siddique, R. H.; Donie, Y. J.; Gomard, G.; Yalamanchili, S.; Merdzhanova, T.; Lemmer, U.; Hölscher, H. Bioinspired Phase-Separated Disordered Nanostructures for Thin Photovoltaic Absorbers. *Sci. Adv.* **2017**, *3*, No. e1700232.
- (33) Donie, Y. J.; Smeets, M.; Egel, A.; Lentz, F.; Preinfalk, J. B.; Mertens, A.; Smirnov, V.; Lemmer, U.; Bittkau, K.; Gomard, G. Light Trapping in Thin Film Silicon Solar Cells via Phase Separated Disordered Nanopillars. *Nanoscale* **2018**, *10*, 6651–6659.
- (34) Hossain, I. M.; Donie, Y. J.; Schmager, R.; Abdelkhalik, M. S.; Rienäcker, M.; Wietler, T. F.; Peibst, R.; Karabanov, A.; Schwenzer, J. A.; Moghadamzadeh, S.; Lemmer, U.; Richards, B. S.; Gomard, G.; Paetzold, U. W. Nanostructured Front Electrodes for Perovskite/c-Si Tandem Photovoltaics. *Opt. Express* **2020**, *28*, 8878–8897.
- (35) Jiao, B.; Yu, Y.; Dai, Y.; Hou, X.; Wu, Z. Improvement of Light Extraction in Organic Light-Emitting Diodes Using a Corrugated Microcavity. *Opt. Express* **2015**, *23*, 4055–4064.
- (36) Huang, T.-T.; Wu, W. Inkjet-Printed Wearable Nanosystems for Self-Powered Technologies. *Adv. Mater. Interfaces* **2020**, *7*, 2000015.
- (37) Cummins, G.; Desmulliez, M. P. Inkjet Printing of Conductive Materials: A Review. *Circuit World* **2012**, *38*, 193–213.
- (38) Huang, C. *Phase Separation in Thin Polymer Films: From Self-Stratification to Polymer Blend Lithography*, 1st ed.; Technische Universität Darmstadt: Darmstadt, 2015; pp 1–135.
- (39) Geveke, D. J.; Danner, R. P. Ternary Phase Equilibria of Polystyrene with a Second Polymer and a Solvent. *J. Appl. Polym. Sci.* **1993**, *47*, 565–575.
- (40) Lau, W. W.; Burns, C. M.; Huang, R. Y. Interaction Parameters in Mixtures of Polystyrene-Poly (methyl Methacrylate)-Toluene. *Eur. Polym. J.* **1987**, *23*, 37–39.
- (41) Tanaka, K.; Takahara, A.; Kajiyama, T. Film Thickness Dependence of the Surface Structure of Immiscible Polystyrene/Poly (methyl Methacrylate) Blends. *Macromolecules* **1996**, *29*, 3232–3239.
- (42) Li, L.; Sosnowski, S.; Chaffey, C. E.; Balke, S. T.; Winnik, M. A. Surface Morphology of a Polymer Blend Examined by Laser Confocal Fluorescence Microscopy. *Langmuir* **1994**, *10*, 2495–2497.
- (43) Bates, F. S. Polymer-Polymer Phase Behavior. *Science* **1991**, *251*, 898–905.
- (44) Abyzov, A. S.; Schmelzer, J. W. Nucleation versus Spinodal Decomposition in Confined Binary Solutions. *J. Chem. Phys.* **2007**, *127*, 114504.
- (45) Favvas, E.; Mitropoulos, A. C. What Is Spinodal Decomposition. *J. Eng. Sci. Technol. Rev.* **2008**, *1*, 25–27.
- (46) Binder, K.; de Gennes, P.-G.; Giannelis, E.; Grest, G.; Hervet, H.; Krishnamoorti, R.; Leger, L.; Manias, E.; Raphael, E.; Wang, S.-Q. *Polymers in Confined Environments*, 1st ed.; Springer: Berlin, 1999; Vol. 138, pp 1–89.
- (47) Li, X.; Han, Y.; An, L. Annealing Effects on the Surface Morphologies of Thin PS/PMMA Blend Films with Different Film Thickness. *Appl. Surf. Sci.* **2004**, *230*, 115–124.
- (48) Donev, A.; Torquato, S.; Stillinger, F. H. Pair Correlation Function Characteristics of Nearly Jammed Disordered and Ordered Hard-Sphere Packings. *Phys. Rev. E* **2005**, *71*, 011105.

- (49) Silva, G. G.; de Freitas Rocha, P. M.; de Oliveira, P. S.; Neves, B. R. A. Domain Size Effects on the Thermal Properties of PS/PMMA Blends. *Appl. Surf. Sci.* **2004**, *238*, 64–72.
- (50) You, J.; Shi, T.; Liao, Y.; Li, X.; Su, Z.; An, L. Temperature Dependence of Surface Composition and Morphology in Polymer Blend Film. *Polymer* **2008**, *49*, 4456–4461.
- (51) Ye, S.; Cao, Y.; Feng, J.; Wu, P. Temperature-Dependent Compatibilizing Effect of Graphene Oxide as a Compatibilizer for Immiscible Polymer Blends. *RSC Adv.* **2013**, *3*, 7987–7995.
- (52) Voorhees, P. W. The Theory of Ostwald Ripening. *J. Stat. Phys.* **1985**, *38*, 231–252.
- (53) Zhan, Z.; An, J.; Wei, Y.; Du, H. Inkjet-Printed Optoelectronics. *Nanoscale* **2017**, *9*, 965–993.
- (54) Li, Y.; Kovačič, M.; Westphalen, J.; Oswald, S.; Ma, Z.; Hänisch, C.; Will, P.-A.; Jiang, L.; Junghaehnel, M.; Scholz, R.; Lenk, S.; Reineke, S. Tailor-Made Nanostructures Bridging Chaos and Order for Highly Efficient White Organic Light-Emitting Diodes. *Nat. Commun.* **2019**, *10*, 1–11.
- (55) Lequin, R. M. Enzyme Immunoassay (EIA)/Enzyme-Linked Immunosorbent Assay (ELISA). *Clin. Chem.* **2005**, *51*, 2415–2418.
- (56) Schwab, P. M.; Moosmann, C.; Wissert, M. D.; Schmidt, E. W.-G.; Ilin, K. S.; Siegel, M.; Lemmer, U.; Eisler, H.-J. Linear and Nonlinear Optical Characterization of Aluminum Nanoantennas. *Nano Lett.* **2013**, *13*, 1535–1540.